J. Fluid Mech. (1990), *vol.* 216, *pp.* 381–410
Printed in Great Britain

A sphere in shear flow at finite Reynolds number: effect of shear on particle lift, drag, and heat transfer

By DAVID S. DANDY[1] AND HARRY A. DWYER[2]
[1] Combustion Research Facility, Sandia National Laboratories, Livermore, CA 94551, USA
[2] Department of Mechanical Engineering, University of California, Davis, CA 95616, USA

(Received 2 March 1989)

Three-dimensional numerical solutions have been obtained for steady, linear shear flow past a fixed, heated spherical particle over a wide range of Reynolds number ($0.1 \leqslant R \leqslant 100$) and dimensionless shear rates ($0.005 \leqslant \alpha \leqslant 0.4$). The results indicate that at a fixed shear rate, the dimensionless lift coefficient is approximately constant over a wide range of intermediate Reynolds numbers, and the drag coefficient also remains constant when normalized by the known values of drag for a sphere in uniform flow. At lower values of the Reynolds number, the lift and drag coefficients increase sharply with decreasing R, with the lift coefficient being directly proportional to $R^{-\frac{1}{2}}$. For the range of shear rates studied here, the rate of heat transfer to the particle surface was found to depend only on the Reynolds number, that is, it was insensitive to the shear rate. The dimensionless rate of heat transfer, the Nussel number Nu, was seen to increase monotonically with R.

1. Introduction

The transport of particles and drops plays an important role in many combustion processes, and as a consequence a great deal of experimental work has been done to study the effects of the coupling between fluid flow, heat and mass transfer and drop shape. An extensive review of both theoretical and experimental work is given by Clift, Grace & Weber (1978). All of the theoretical work done thus far on drops and particles at finite Reynolds numbers has been limited to the case where the outer flow field is assumed to be axisymmetric, thereby reducing the computational domain to two dimensions. Approximate solutions have been obtained for drops in the limit of very small deformation for either high (Moore 1959, 1963, 1965; Harper & Moore 1968; Harper 1972) or low (Taylor & Acrivos 1964; Brignell 1973) Reynolds number. Numerical solutions for drops and particles at finite Reynolds numbers have either required that the body remain spherical in shape (Masliyah 1970; Woo 1971; Brabston & Keller 1975; LeClair *et al.* 1972; Rivkind & Ryskin 1976; Oliver & Chung 1987; Fornberg 1988), or deform to shapes not too far-removed from spherical (Ryskin & Leal 1984*a*, *b*; Christov & Volkov 1985; Dandy & Leal 1989), but all have assumed that the flow is uniform and the domain is infinite in extent.

A more realistic situation is for the particle or drop to be moving in the presence of an obstacle such as a wall, which will influence the flow field around the particle. For flow past a planar surface, to leading order the flow near the wall is a simple shear flow, and thus any particle present in this region would experience a linear flow field, with the fluid velocity going to zero at the wall. The non-uniformity of this flow results in a force imbalance on the particle surface in the direction normal to the wall, causing the particle to drift away from the wall. The drag (that is, the force on the particle in the direction of the bulk fluid motion) would also be affected by the non-uniform velocity distribution in the surrounding fluid. Previous investigations of particle migration have relied on the assumption that the Reynolds number be small, such that Stokes flow is the first-order approximation of the flow solution. It is necessary for the Reynolds number to be non-zero for any lift to occur, and Bretherton (1962) proved that, if the inertia terms in the equations of motion are neglected, no lift force can exist for a body of revolution in a unidirectional flow. Rubinow & Keller (1961) and Saffman (1965) both used asymptotic expansions to obtain inertial corrections for small but non-zero values of the Reynolds number for the case of a single sphere in an unbounded flow domain. Saffman (1965) considered the case of a solid sphere rotating at a constant angular velocity, and translating at a constant velocity relative to the local undisturbed uniform shear flow. To take into account the effects of boundaries and to allow for the sphere to be neutrally buoyant, Cox & Brenner (1968) studied a three-dimensional Poiseuille flow problem using matched asymptotic expansions to solve for the flow-induced force and torque on the sphere. In addition to assuming that the particle and channel Reynolds numbers were small, Cox & Brenner (1968) also assumed that the ratio of the sphere radius to the tube radius was small. Their solutions could not be presented in explicit form, so Ho & Leal (1974) used a method very similar to Cox & Brenner's to obtain explicit solutions. Ho & Leal restricted their analysis to flows between two infinite plane boundaries, and the two flows they considered were simple shear and Poiseuille. O'Neill (1968) obtained a solution for the force and torque on a sphere in contact with a plane boundary, under the action of a linear shear flow. Later, White *et al.* (1976) used a method similar to that of O'Neill (1968) to study grain saltation in the Martian atmosphere. Schonberg, Drew & Belfort (1986) used singular perturbation techniques to examine interactions between many spherical particles in Poiseuille flow, while removing the restriction that the channel Reynolds number be small but still maintaining a small particle Reynolds number. Schonberg & Hinch (1989) again used singular perturbation expansions, and relaxed the high channel Reynolds number condition of Schonberg *et al.* (1986) to examine particle migration at intermediate channel Reynolds numbers.

As crucial as inertia is for particle migration, no analysis for particles or drops in shear flows at finite Reynolds number have been published, primarily due to the necessity of using numerical techniques to study the three-dimensional nature of the system. This flow problem is important, and is the first step in the study of the motion and breakup of droplets in shearing flows at finite Reynolds number. Further, it provides the opportunity to study three-dimensional flow separation, and its relation to surface stress and vorticity.

The goals of this work are to study the coupling between flow type (the Reynolds number R and the dimensionless shear rate α), the resulting steady velocity and pressure fields, and heat transfer characteristics in order to quantify the relationship between the computed values of C_L, C_D, the Nusselt number Nu, and the characteristics of the flow, R and α. Steady solutions will be presented at a range of Reynolds numbers spanning three orders of magnitude, $0.1 \leqslant R \leqslant 100$, and dimensionless shear rates covering almost two orders of magnitude, $0.005 \leqslant \alpha \leqslant 0.4$.

To obtain numerical solutions to this problem, a spherical-type, boundary-fitted coordinate grid is used in the discretization of the flow domain. The grid generation technique was developed for construction of general, three-dimensional, boundary-

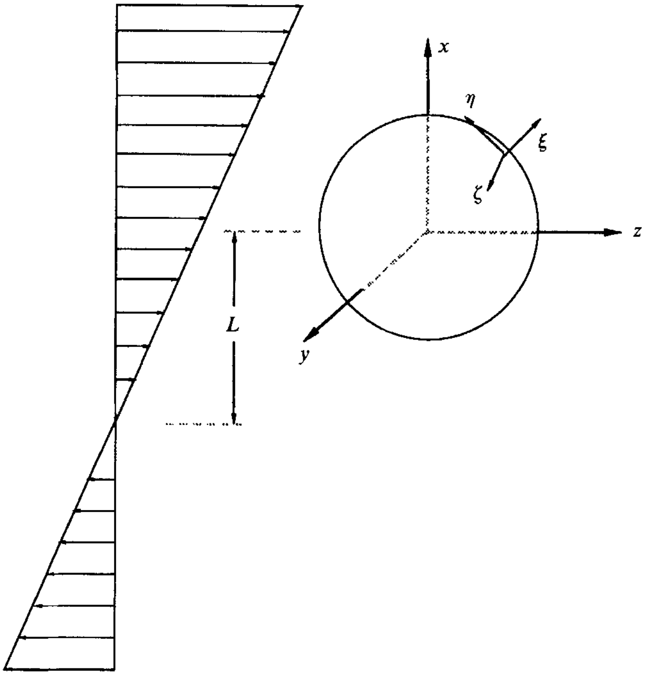

FIGURE 1. Schematic of the problem. The imposed flow is a linear shear flow, and is described by $\boldsymbol{U}_\infty = (U_\infty + \tilde{\alpha}x)\,\boldsymbol{e}_z$.

fitted, non-orthogonal grids for use in free-surface problems; in the present study the grid reduces to an orthogonal, spherical-type one. The full Navier–Stokes equations and the thermal energy equation are approximated on this grid using a recently developed finite-volume formulation, described below, that is capable of accurately resolving time-dependent, three-dimensional flows.

2. Problem statement and numerical approach

A cold particle of temperature T_p is held fixed in a hot fluid of temperature T_∞. We assume that the particle is spherical, with radius a, and is rigid such that it has a no-slip surface. The particle is constrained so that it can neither translate nor rotate. The undisturbed local fluid velocity (that is, the flow field in the absence of the particle) is a simple shear flow. It is assumed that the fluid is incompressible, and that the fluid properties are independent of temperature, allowing the fluid to be characterized by the constant parameters density ρ, viscosity μ, and thermal diffusivity κ. As shown in figure 1, the geometry of this system is represented by the Cartesian coordinates (x, y, z), and the boundary-fitted coordinate system is represented by the general coordinates (ξ, η, ζ), where the ξ is radial, and η and ζ are of angular-type. Note that the origin of the frame of reference is fixed at the centre of the particle. The angular coordinate η has a value of zero at the outflow axis, and a value of unity at the inflow axis, while ζ is zero on the high-velocity side of the particle $(x^2+z^2 = 1, x > 0, y = 0)$ and unity on the low-velocity side $(x^2+z^2 = 1, x < 0, y = 0)$. The undisturbed flow is described

$$\boldsymbol{U}_\infty = (U_\infty + \tilde{\alpha}x)\,\boldsymbol{e}_z,$$

where U_∞ is the centreline velocity, and $\tilde{\alpha}$ is the dimensional shear rate. Note that the vorticity in the free stream, given by $\boldsymbol{\omega} = \nabla \times \boldsymbol{U}_\infty$ has one component, $\tilde{\alpha}\boldsymbol{e}_y$. Therefore, the magnitude of the lone component of vorticity in the undisturbed flow is equal to the shear rate.

2.1. *Governing equations and boundary conditions*

The equations describing the fluid motion and heat transfer are the continuity equation, the Navier–Stokes equations, and the thermal energy equation, written in integral form, and stated with respect to a frame of reference fixed at the centre of the particle. In the present work the three equations, along with all associated boundary conditions, are non-dimensionalized using the radius a of the spherical particle as a characteristic length, the centreline velocity U_∞ as a characteristic velocity, T_∞ as a characteristic temperature, and ρU_∞^2 as the pressure scale. Note that, in steady head transfer problems (such as this one) where T_p is constant, it is the convention to define a dimensionless temperature

$$T = (T' - T_\infty)/(T_\mathrm{p} - T_\infty),$$

so that $0 \leqslant T \leqslant 1$. Here, however, we have chosen $T = T'/T_\infty$ as the dimensionless temperature. The reason for this choice is simply that the numerical technique used in this work was developed for the more general case of the unsteady heat-up of a particle or drop, for which T_p does not remain constant. This convention is common in the heat transfer and combustion literature, and was used here to remain consistent with future work. The dimensionless forms of the governing equations are then

$$\frac{\partial}{\partial t}\iiint_{\mathscr{V}} \mathrm{d}V + \iint_{\mathscr{S}} \boldsymbol{u}\cdot\boldsymbol{n}\,\mathrm{d}A = 0, \tag{1}$$

$$\frac{\partial}{\partial t}\iiint_{\mathscr{V}} \boldsymbol{u}\,\mathrm{d}V + \iiint_{\mathscr{V}} \boldsymbol{u}\cdot\nabla\boldsymbol{u}\,\mathrm{d}V = -\iint_{\mathscr{S}} p\boldsymbol{n}\,\mathrm{d}A + \frac{2}{R}\iint_{\mathscr{S}} \boldsymbol{n}\cdot\boldsymbol{\tau}\,\mathrm{d}A, \tag{2}$$

and

$$\frac{\partial}{\partial t}\iiint_{\mathscr{V}} T\,\mathrm{d}V + \iiint_{\mathscr{V}} \boldsymbol{u}\cdot\nabla T\,\mathrm{d}V = \frac{2}{RP}\iint_{\mathscr{S}} (\nabla T)\cdot\boldsymbol{n}\,\mathrm{d}A, \tag{3}$$

where the velocity vector is $\boldsymbol{u} = (u, v, w)$ (corresponding to the Cartesian Coordinates (x, y, z)), p is pressure, $\boldsymbol{\tau}$ is the viscous sress tensor, T is temperature, the Reynolds number is $R = 2\rho a U_\infty/\mu$, and the Prandtl number is $P = \nu/\kappa$, where ν is the kinematic viscosity, μ/ρ. Although all operators and geometric quantities in these equations will be evaluated using the curvilinear coordinates (ξ, η, ζ), the Cartesian components of $\boldsymbol{u}$ will be considered in order to guarantee orthogonality of the three velocity components. Equations (1)–(3) are written with the time derivative outside of the integral sign, because the coordinate grid is invariant with time in this formulation. However, for a moving-boundary problem such as a deforming drop, it would be necessary to take into account the time-dependent nature of the coordinate mapping. Further, although we seek steady solutions, all three of these equations are written in a time-dependent form because of the specific solution algorithm used in this work. This point will be discussed further in §2.2. The assumption of incompressibility and constant properties allows the formation of dimensionless groups R and P in front of the viscous and diffusive terms in equations (2) and (3), respectively.

The velocity boundary condition upstream of the particle at infinity in dimensionless form is

$$\boldsymbol{u} \rightarrow (1+\alpha x)\,\boldsymbol{e}_z, \tag{4a}$$

where the coordinates x, y, and z have been non-dimensionalized by the particle radius a, the shear rate has been non-dimensionalized by U_∞/a, and the fluid temperature is non-dimensionalized to unity. Note that the undisturbed fluid velocity goes to zero at a distance $x = -\alpha$ from the particle centre (the length L in figure 1). At the particle surface the velocity must be zero:

$$\boldsymbol{u} = 0. \tag{4b}$$

The particle is assumed to be isothermal. For the purposes of this work, the dimensionless particle temperature, (T_p/T_∞), is taken as 0.1, since this value is representative of a cold particle introduced into a hot combusion environment.

The computational domain for this problem is described by the general curvilinear coordinates ξ, η, and ζ with the conditions (4a, b) applied at the boundaries of these coordinates as follows. The surface of the particle corresponds to $\xi = 0$, while the boundary at infinity corresponds to $\xi = 1$. The calculations presented in this paper were performed on a mesh having an outer boundary located at $\hat{L} = [x^2+y^2+z^2]^{\frac{1}{2}} =$ 25 radii. The boundary conditions at $\xi = 0$ are then $\boldsymbol{u} = 0$ and $T = 0.1$. Application of the boundary conditions at $\xi = 1$ is more complicated, and will be discussed below. The outflow axis (positive z-axis) corresponds to $\eta = 0$, and the upstream axis (negative z-axis) corresponds to $\eta = 1$. These are both symmetry axes for this problem, and as such, no-flux boundary conditions can be imposed on all dependent variables. That is, $\partial \boldsymbol{u}/\partial \eta = \partial T/\partial \eta = 0$ at $\eta = 0$, 1. The (x, z)-plane is a symmetry plane (owing to particle symmetry), and therefore it is only necessary to solve the governing equations in a half-space on one side of this plane. (This will be discussed further in §3.1.) As a consequence, the final coordinate variable ζ is applied over half of the total domain, and as such, symmetry conditions can be applied at the boundaries of ζ. These conditions are then $\partial \boldsymbol{u}/\partial \zeta = \partial T/\partial \zeta = 0$. For the more general case of a non-planar-symmetric particle it is necessary to start and end ζ at the same location, so that the particle is completely circumscribed by the coordinate mesh; the algorithm used here has been developed to handle either situation.

Since the outer boundary of the domain ($\xi = 1$) is located at a finite distance from the particle surface, it is not correct to impose the far-field conditions on velocity and temperature at every point on this boundary, particularly downstream of the particle in the region where η is small. Therefore, the boundary conditions at $\xi = 1$ are applied in two different ways: for $\eta \geqslant 0.5$ (the midpoint), the upstream conditions on velocity and temperature are imposed, while for $\eta < 0.5$ it is assumed that the variables are invariant with respect to z, that is, the velocity field and the isotherms are approximately parallel to the z-direction. This assumption is valid over a wide range of Reynolds numbers, breaking down only in the limit of very small values of $R (R \ll 1)$. Further, the volume of the particle is only 0.0064% of the volume of the computational domain, and any disturbances in the flow field caused by the presence of the particle will be extremely weak when they have propagated to the outer boundary.

Once the steady velocity, pressure, and temperature fields have been calculated for specified values of R, α, and P, it is desirable to compute the forces on the particle and the rate of heat transfer to the particle surface. The drag and lift are the components of the fluid force on the particle surface in the z- and x-directions, respectively, and in dimensional form, are defined by

$$\left.\begin{aligned} F_D &= -\iint_{\mathscr{S}} p\boldsymbol{e}_z\cdot\boldsymbol{n}\,\mathrm{d}A + \iint_{\mathscr{S}} \boldsymbol{n}\cdot\boldsymbol{\tau}\cdot\boldsymbol{e}_z\,\mathrm{d}A, \\ F_L &= -\iint_{\mathscr{S}} p\boldsymbol{e}_x\cdot\boldsymbol{n}\,\mathrm{d}A + \iint_{\mathscr{S}} \boldsymbol{n}\cdot\boldsymbol{\tau}\cdot\boldsymbol{e}_x\,\mathrm{d}A, \end{aligned}\right\} \tag{5}$$

where $\boldsymbol{n}$ is the outward-pointing unit normal vector at the particle surface, and $\boldsymbol{\tau}$ is the viscous stress tensor. The non-dimensional drag and lift are then

$$C_D = \frac{F_D}{\frac{1}{2}\rho U_\infty^2 \pi a^2}, \quad C_L = \frac{F_L}{\frac{1}{2}\rho U_\infty^2 \pi a^2}. \tag{6}$$

The lift coefficient C_L would be zero for the case of uniform streaming flow, and the fact that it will assume non-zero values here demonstrates the force imparted to the particle due to the presence of a zero velocity point, for example, a wall.

The rate of heat transfer to the particle surface is computed by integrating the heat flux over the surface of the sphere (using dimensional quantities):

$$\begin{aligned} Q &= -\iint_{\mathscr{S}} \boldsymbol{q}\cdot\boldsymbol{n}\,\mathrm{d}A \\ &= k\iint_{\mathscr{S}} (\nabla T)\cdot\boldsymbol{n}\,\mathrm{d}A, \end{aligned} \tag{7}$$

where k is the thermal conductivity of the surrounding fluid. The rate of heat transfer can also be expressed as $Q = h(4\pi a^2)(T_\mathrm{p} - T_\infty)$, where h is the film heat transfer coefficient. The Nusselt number Nu is then defined as

$$Nu = \frac{2ah}{k} = \frac{1}{2\pi a(T_\mathrm{p} - T_\infty)}\iint_{\mathscr{S}} (\nabla T)\cdot\boldsymbol{n}\,\mathrm{d}A. \tag{8}$$

The Nusselt number is the dimensionless rate of heat transfer, and can be viewed as the average temperature gradient in the fluid, evaluated over the heat transfer surface (that is, the particle surface).

2.2 *Method of solution*

To obtain solutions for $\boldsymbol{u}(\xi, \eta, \zeta)$, $p(\xi, \eta, \zeta)$ and $T(\xi, \eta, \zeta)$ in the domain $0 \leqslant \xi, \eta, \zeta \leqslant 1$, the governing equations, are approximated at discrete points in the domain, and the resulting coupled set of algebraic equations is solved for the dependent variables. The three coordinate directions ξ, η and ζ are divided into M_ξ, M_η, and M_ζ points, respectively, and the equations are then evaluated at each of these $M_\xi \times M_\eta \times M_\zeta$ points. Figure 2(*a*) shows a typical volume element resulting from the spatial discretization of the domain. The index i denotes the ζ-direction, j denotes the η-direction, and k denotes the ξ-direction. The sides of the rectangular volume element are located at the approximate midpoints between the node (ijk) and its six nearest neighbours.

The volume integrals in (2) and (3) are computed in each cell by evaluating each integrand at the cell centre, that is, at the node (ijk), and multiplying by the volume

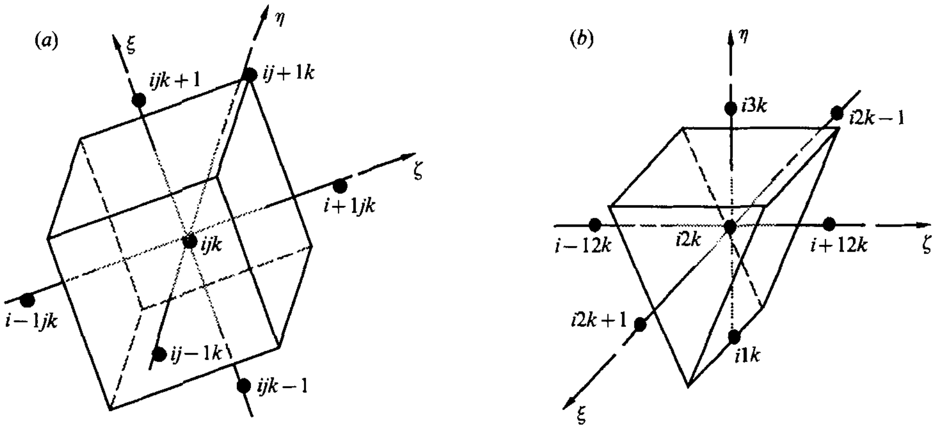

FIGURE 2. Representative volume elements arising from discretization of the computational domain; (*a*) rectangular volume element centred at the node (*ijk*), and (*b*) triangular volume element centred at the node (*i*2*k*).

of the element. The base vectors in the curvilinear coordinate system are used to compute the volume:

$$V_{ijk} = (\boldsymbol{e}_{\zeta} \times \boldsymbol{e}_{\eta}) \cdot \boldsymbol{e}_{\xi}, \tag{9}$$

where the three base vectors are evaluated at the point (*ijk*). To compute the differential operators appearing in the governing equations, it is only necessary to evaluate geometric quantities of the volume element: For example, the three components of the gradient operator in the second term of (2) are

$$\boldsymbol{\nabla}_{\zeta} = \frac{\boldsymbol{e}_{\eta} \times \boldsymbol{e}_{\xi}}{V_{ijk}}, \quad \boldsymbol{\nabla}_{\eta} = \frac{\boldsymbol{e}_{\xi} \times \boldsymbol{e}_{\zeta}}{V_{ijk}}, \quad \boldsymbol{\nabla}_{\xi} = \frac{\boldsymbol{e}_{\zeta} \times \boldsymbol{e}_{\eta}}{V_{ijk}}, \tag{10}$$

where V_{ijk} is computed in (9).

The surface integrals are computed in a similar manner, except that they must be evaluated on all six faces for each rectangular cell. All surface integrands are computed at the midpoint of each face, multiplied by the area of that face, and then summed with the contributions from the other faces. Linear interpolation is used to evaluate the variables, operators, and geometric properties on each face.

Owing to the nature of the curvilinear coordinate system, the boundaries $\eta = 0$ and $\eta = 1$ are lines rather than surfaces. Because of this feature, the volume elements adjacent to the lines $\eta = 0$, 1 for all ξ and ζ are triangular in shape. (These elements can be thought of as six-sided, with one of the surfaces having zero area.) Therefore, the approximations to (2) and (3) at the nodes ($i2k$) and ($iM_{\eta}-1k$), $1 < i < M_{\zeta}$, $1 < k < M_{\xi}$ must use a five-sided volume element (shown in figure 2*b*). The surface and volume integrals are computed in a manner analogous to those for the six-sided elements.

From the approximations of the four governing equations arising from (2) and (3) at each of the $(M_{\xi}-2) \times (M_{\eta}-2) \times (M_{\zeta}-2)$ interior volume elements, and the addition of the equations arising from application of the boundary conditions at the remaining boundary elements, a set of $4 \times M_{\xi} \times M_{\eta} \times M_{\zeta}$ equations and $5 \times M_{\xi} \times M_{\eta} \times M_{\zeta}$ unknowns is obtained, in which the additional set of unknowns is the pressure field p. Because the problem is underdetermined, the equations must be solved in an iterative manner, using the continuity equation, (1), as the additional constraint on the system. The iteration algorithm is described in detail elsewhere (Dwyer 1989), and here it will suffice to state that in the algorithm the pressure is held fixed while the velocity and temperature fields are computed using (2) and (3), and then the pressure is computed using the continuity equation and the current approximation to the velocity field. This successive approximation algorithm is repeated until convergence. This pressure correction algorithm is closely related to the artificial compressibility method of Chorin (1967, 1968).

For fixed values of the pressure, the velocity and temperature fields are computed iteratively using a predictor/corrector updating method analogous to the Alternating Direction Implicit (ADI) scheme of Peacemann & Rachford (1955). The three velocity components and the temperature are iterated in uncoupled form using the predictor/corrector scheme; the nonlinear terms appearing in (2) are treated explicitly, thereby reducing the algebraic equations to a linear form.

In the results presented below, the number of nodes used is $M_\xi = 55$, $M_\eta = 41$, and $M_\zeta = 31$. This discretization yields a total of 69905 nodes in the domain. There are five unknowns at each node ($\boldsymbol{u}$, p, T), for a total of almost 350000 unknowns. Fifty-five nodes are used in the ξ-direction because the domain extends 25 radii from the particle centre. A skewing factor in the grid generation scheme provides a high density of nodes near the particle surface ($\xi = 0$), with the internode spacing increasing with ξ; the skewing factor is simply $(\xi_{i+1} - \xi_i) = 1.1(\xi_i - \xi_{i-1})$. The nodes in the η- and ζ-directions are evenly spaced; more nodes are used for η than ζ because gradients are expected to be higher in the η-direction. To save computer time during a run, metric quantities were computed once and then stored for the duration of the run. The penalty in doing this is the necessity of having a large memory available, but the computations were performed on a CRAY-2, so memory was not a consideration.

All calculations were started with a dimensionless time step of $\Delta t = 0.001$, and Δt was gradually increased to $O(10^{-2})$ by the end of a simulation. Normally, 200–300 time steps were required to reach a steady-state solution. Each time step took about 15 cpu s on a CRAY-2. The exact cpu requirements depended on the number of pressure correction interations done at each time step. Calculations were terminated when

$$\max_{i,j,k} |\tilde{p}_{ijk}| \leqslant 10^{-5},$$

where $\tilde{p}_{ijk}$ is the residual of the pressure correction at the node (ijk), and when (1) was satisfied in all elements to within 1 part in 10^5. The drag, lift, and heat flux were computed at each time step, and a run was not halted until the values changed by less than one part in 10^6 per time step.

3. Results and discussion

Calculations were performed for Reynolds numbers in the range $0.1 \leqslant R \leqslant 100$ and values of the shear rate in the range $0.005 \leqslant \alpha \leqslant 0.4$. This range of Reynolds numbers was chosen as characteristic of the values of R that a small fuel drop or coal particle would experience during combustion; fuel droplets typically enter a combusion chamber with Reynolds numbers of $O(10^2)$, and as they decrease in diameter and velocity during the process of burning, R continuously decreases, reaching values of less than unity. The shear rate $\alpha = 0.4$ was chosen as an upper bound for the calculations because it yields a change in velocity of more than 100%

from the low-velocity side ($x = -1$) to the high-velocity side of the particle ($x = 1$). In dimensional terms, if we assume that we have a 100-μm particle in air, centreline velocities presented here range from approximately 1.5 cm/s to 1700 cm/s, and shear rates range from 0.5 s^{-1} to 67000 s^{-1}. Runs were not performed below $\alpha = 0.005$, because the flow structure was nearly axisymmetric at this small rate of shear. Further, the magnitude of the lift force on the particle at this shear rate is comparable to the discretization error. Thus, while results for drag and heat transfer are reliable at low shear rates, those for lift cannot be considered accurate for $\alpha < 0.005$.

To study the heat transfer characteristics of these shear flows at various values of R and α decoupled from the physical properties of the fluid surrounding the particle, all of the runs were carried out at $P = 1$, that is, the kinematic viscosity is set equal to the thermal diffusivity of the fluid, and this value for P is reasonable for many gases. (The Prandtl number for many gases lies in the range $0.6 \leqslant P \leqslant 0.85$.)

3.1. *Accuracy*

The results and conclusions presented below rely on the accuracy of the numerical calculations. It is especially important to verify the accuracy of the results since the numerical technique used here is new, and has never before been tested on three-dimensional problems.

The scheme employed here to approximate gradients is analogous to centred differencing in a finite-difference scheme, and it has been documented that unphysical oscillatory behaviour can occur in regions where convection dominates diffusion, when second-order, centred differencing is used for the convective terms (Roache 1972, pp. 161–165). While this phenomenon is more common at Reynolds numbers on the order of several hundred, it has been observed that the pressure field is sensitive to the type of difference operator employed, even at modest values of the Reynolds number. To investigate the effect of cell Reynolds number on the flow solutions, we performed calculations at $R = 70$, $\alpha = 0.2$ for three different grid densities: $(M_\xi, M_\eta, M_\zeta) = (21, 21, 21)$, $(41, 31, 21)$, and $(55, 41, 31)$. A steady solution could not be computed on the coarsest grid, regardless of the initial guess. We believe that the (21, 21, 21) grid cannot adequately resolve gradients in the streamwise and radial directions, and as a result the pressure near the body oscillates in time with growing amplitude. A similar situation was encountered using the second grid, (41, 31, 21), but when extreme under-relaxation was used in the pressure correction algorithm, the solution did converge. Although the solutions for drag, lift, and heat transfer on this grid matched the solutions on the (55, 41, 31) grid to within several percent, the relative instability of the run led us to use the finer mesh for all calculations. For all cases considered, solutions computed on the (55, 41, 31) mesh were stable and smooth.

Four tests were done to examine the sensitivity of the solution to the position of the outer boundary. Using the same values of R and α as above, and the (55, 41, 31) grid, we computed solutions for $\hat{L} = 10$, 15, 20, and 25 radii. The scheme converged smoothly for all four cases, and while values for drag and heat transfer were self-consistent (to within 1%) for all cases, the lift on the sphere varied dramatically for different values of $\hat{L}$. For $\hat{L} = 10$, 15 the force on the particle in the transverse direction was actually opposite in sign to what was expected, with the magnitude being largest for $\hat{L} = 10$. Manipulating the grid spacing in the radial direction had little effect on the values of lift for these two cases. However, the transverse forces on the sphere for $\hat{L} = 20$ and 25 were in the (assumed) correct direction, and agreed with one another to within 2%. To minimize the effect of the outer boundary on the flow solution, the value of $\hat{L} = 25$ was used in all subsequent calculations.

It was stated in §2.1 that, while the code was capable of treating an arbitrarily shaped body, it was advantageous to take advantage of the geometrical symmetry of the problem; the (x, z)-plane is a symmetry plane, and the computational space can be reduced to a half-space, or in this case, a half-sphere. Although all of the results presented here were computed in the half-space, two solutions were computed using the full space in order to test the implementation of the periodic boundary conditions for ζ, and more importantly, to ensure that the (x, z)-plane was indeed a symmetry plane for the flow. The two cases considered were computed on a (55, 41, 51) grid, at a shear rate $\alpha = 0.2$ and Reynolds numbers of 1 and 100. This grid was 17% coarser in the ζ-direction than the half-plane grid, and discretization was done in a manner such that for each point located at (x, y, z) there was a corresponding point located at $(x, -y, z)$. Thus, symmetry could be tested by evaluating

$$\frac{|f(x, y, z)| - |f(x, -y, z)|}{|f(x, y, z)|}$$

at steady-state for every point in the domain at which f was non-zero, and for all values of $f = u, v, w, p, T$. For both of the cases examined, this expression always yielded values that were $o(10^{-8})$ at *all* points evaluated in the computational space, indicating that there were no asymmetries present in the steady solutions. The issue of time-dependent, non-symmetric flow behaviour cannot be resolved in the steady-state work done here, but future studies on transient flows will have to use the full space to allow for such asymmetry.

In order to compare our results with accepted results in the literature, we can only look at two limiting cases owing to the fully three-dimensional nature of the flow problem. The first of these cases is the limit of small Reynolds number. Saffman (1965) used matched asymptotic expansions to solve for the lift on a sphere to $O(R^{\frac{1}{2}})$. Saffman assumed that a rigid sphere of radius a translated through a very viscous fluid at a velocity of magnitude U_∞ relative to the velocity of the undisturbed flow passing through the centreline of the sphere, while rotating at an angular speed Ω. The local undisturbed flow field was a simple shear flow, with a shear rate $\tilde{\alpha}$. Saffman's analysis relied on the assumption that three Reynolds numbers defined using U_∞, Ω, and $\tilde{\alpha}$ were all small compared with unity. He found that the dimensional lift on the particle was given by

$$F_L = 6.46\,\mu U_\infty a^2 \tilde{\alpha}^{\frac{1}{2}}/\nu^{\frac{1}{2}} + o(R^{\frac{1}{2}}). \tag{11}$$

Note that to leading order the lift on the particle is independent of its rate of rotation. Non-dimensionalizing (11), we arrive at a form for the lift coefficient in terms of the dimensionless parameters of this problem.:

$$C_L = 5.82\alpha^{\frac{1}{2}}/R^{\frac{1}{2}}, \tag{12}$$

where we have again used U_∞/a to define a non-dimensional shear rate α. To compare the results obtained in this work against the solution of Saffman (1965) shown in (12), the case $R = 0.1$ was considered for six values of α: 0.01, 0.025, 0.05, 0.1, 0.2, and 0.4. When C_L is plotted against $(\alpha/R)^{\frac{1}{2}}$, the relationship should be linear, and this is confirmed in figure 3. The dashed line is the analytical solution of Saffman (1965) and the symbols are the results from this work. The agreement is excellent, except at the smallest value of α, and the explanation for this behaviour has been given above. The agreement between our numerical calculations and (12) is encouraging because we

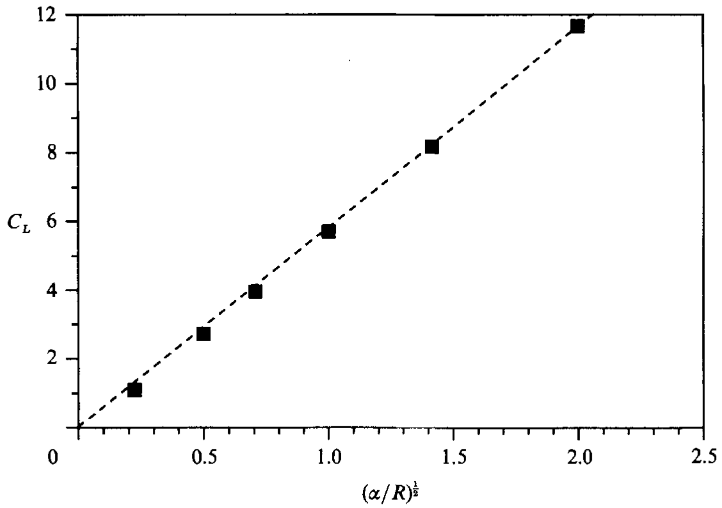

FIGURE 3. Values of the lift coefficient taken from the asymptotic analysis of Saffman (1965) (the dashed line) and results of the present work (the symbols) at $R = 0.1$.

have found in this work that the lift force is a sensitive indicator of any errors in the solution, and further, we expect the outer boundary to exert its greatest effect at low Reynolds numbers owing to the dominance of diffusive forces over inertial forces.

The second limiting case against which we can compare our results is $\alpha = 0$, or, uniform flow. Here, the flow is axisymmetric and numerous examples exist in the literature for the case of a sphere in steady, uniform flow (cf. Clift *et al.* 1978). Although it is computationally expensive to compute two-dimensional flow fields using a three-dimensional formulation, it is nevertheless a viable means of checking the accuracy of the method. For this purpose, results were obtained at $\alpha = 0$ for Reynolds numbers of 10 and 100, and compared with the axsymmetric numerical results of Woo (1971). Figure 4(*b*) shows the surface distribution of pressure computed in this work, and figure 4(*a*) displays the results of Woo (taken from Clift *et al.* 1978). The curves in figure 4(*b*) represent the pressure distributions along the surface line $(\eta, \zeta) = (\eta, 0.5)$, but solutions at all lines of constant ζ on the surface yield the same results. To verify that the numerical results obtained in this work for $\alpha = 0$ are actually axisymmetric, surface contours for heat flux, pressure drag contribution, and viscous drag contribution have been plotted, and two cases, corresponding to $R = 10$ and $R = 100$, are represented in figures 5(*a*) and 5(*b*). The pressure drag and viscous drag contours in figure 5 reflect contributions to the first and second terms, respectively, in the expression for F_D shown in (5). These contours demonstrate the distribution of forces on the particle surface, and should not be confused with contours of pressure and viscous stress. In figure 5, the sphere is being viewed from the side, in the direction normal to the plane of the shear flow, and the flow is left to right. The contours of the z-components of the force, as well as the heat flux, are axisymmetric in character, i.e. the values are independent of ζ. Incidentally, the x-components of force are antisymmetric about the line $\zeta = 0.5$, and the numerical result for the total lift force is less than 10^{-5}.

Finally, properties of the recirculating wake, such as separation angle and wake length, can be computed for the $\alpha = 0$ case and compared against published results for uniform flow. In our calculations, the location of the separation point was

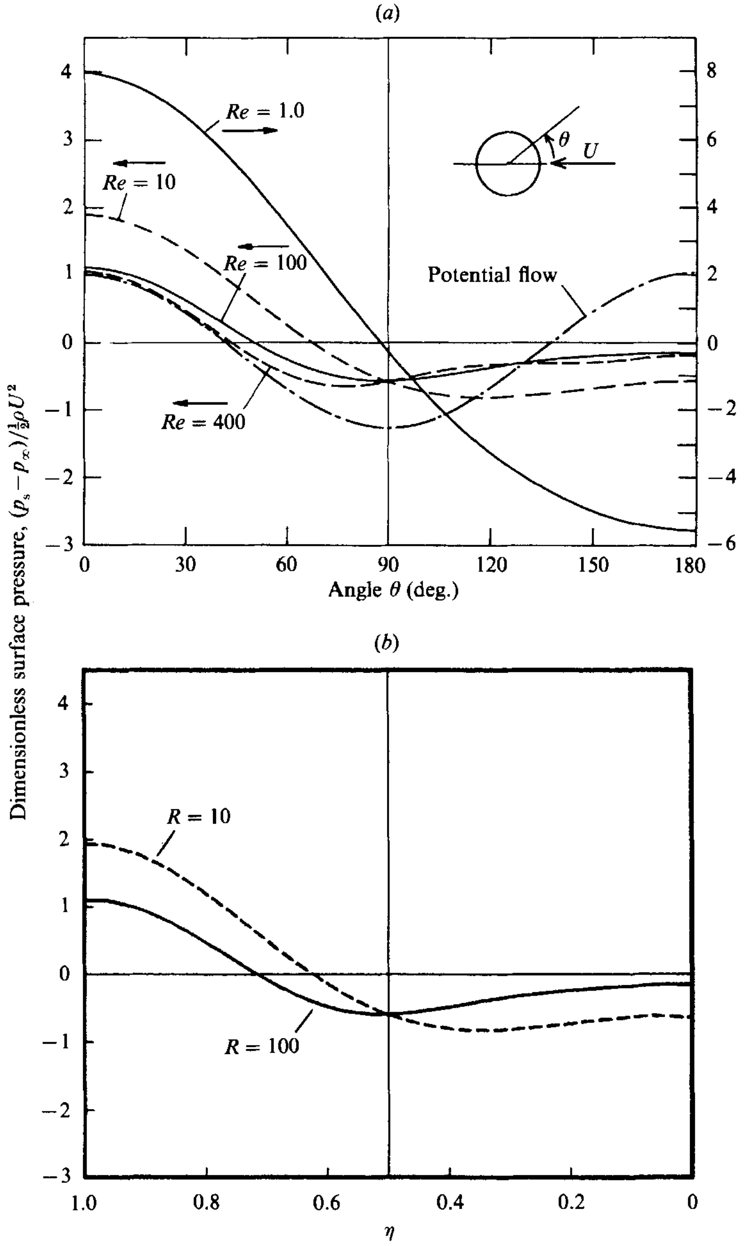

FIGURE 4. Surface distribution of pressure: (a) solution computed by Woo (1971) using a stream function–vorticity formulation; (b) solution computed in this work at $\alpha = 0$.

determined by finding the point on the sphere surface where the shear stress changes sign. (For the axisymmetric case, there is only one component of the surface shear. This will be discussed in more detail later.) The length of the wake was measured by plotting the velocity field in the symmetry plane. Table I shows the results for separation angle and dimensionless wake length (wake length/sphere diameter) for several values of R, compared against equation 5–10 and figure 5.7, respectively, of Clift *et al.* (1978). The results from Clift *et al.* have been compiled from numerous

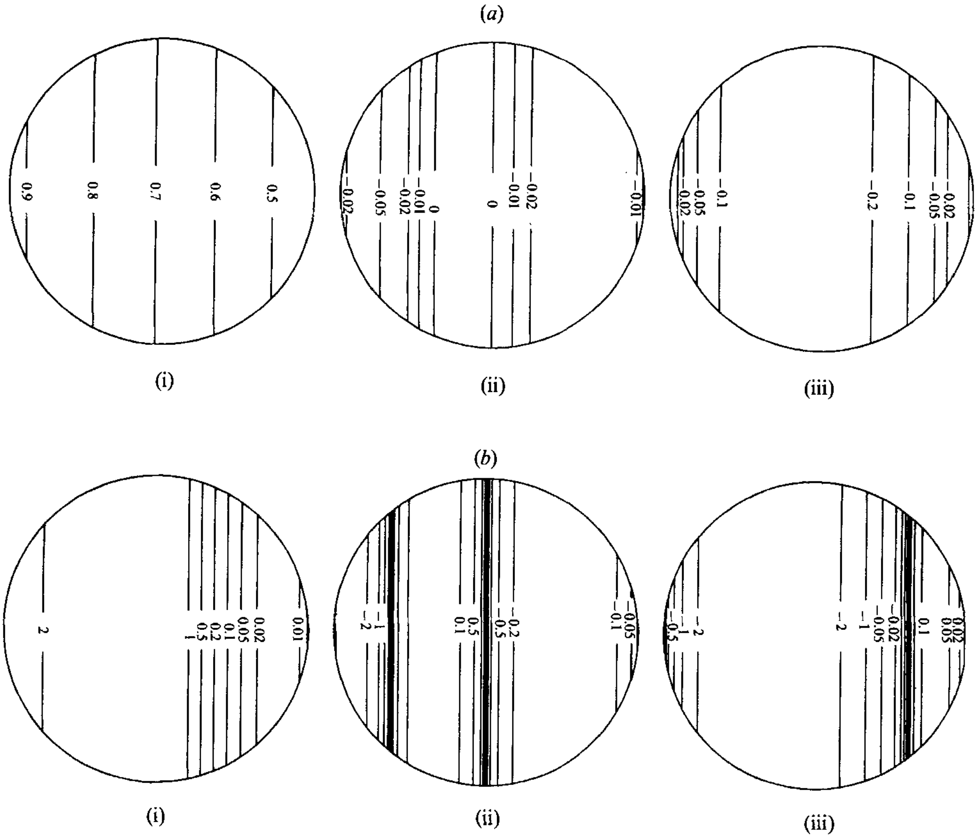

FIGURE 5. Surface contours for (i) the heat flux, (ii) the z-component of the pressure force, and (iii) the z-component of the viscous force, for $\alpha = 0$: (*a*) $R = 10$; (*b*) $R = 100$.

	Separation angle		Dimensionless wake length	
R	Present work	Clift *et al.*	Present work	Clift *et al.*
30	152.2	152.5	0.17	0.18
50	139.1	139.3	0.49	0.49
70	132.5	132.6	0.66	0.67
90	128.3	128.2	0.81	0.82
100	126.7	126.5	0.88	0.89

TABLE 1. Values of separation angle measured from the front stagnation point and dimensionless wake length (wake length/sphere diameter), from Clift *et al.* (1978) and from numerical results of the present work for the case $\alpha = 0$

experimental and theoretical studies. The agreement is excellent for all Reynolds numbers considered.

3.2. *Lift*

It is instructive when examining the lift on the particle to look not only at the total lift force, but also at the two contributions to lift – the pressure contribution and the viscous contribution. (See (5).) These contributions are plotted as a function of R,

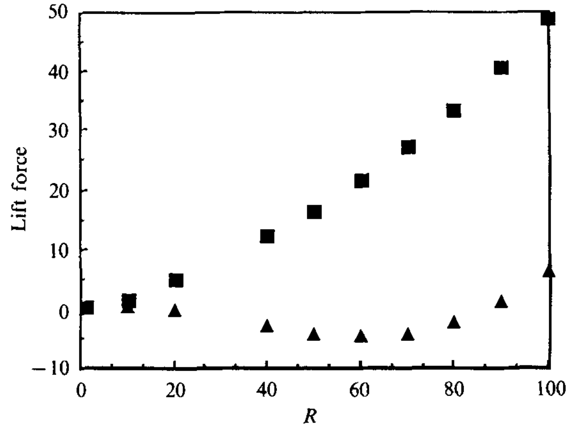

FIGURE 6. The pressure (▲) and viscous (■) contributions to the dimensional lift force on a spherical particle as a function of Reynolds number for the shear rate $\alpha = 0.1$.

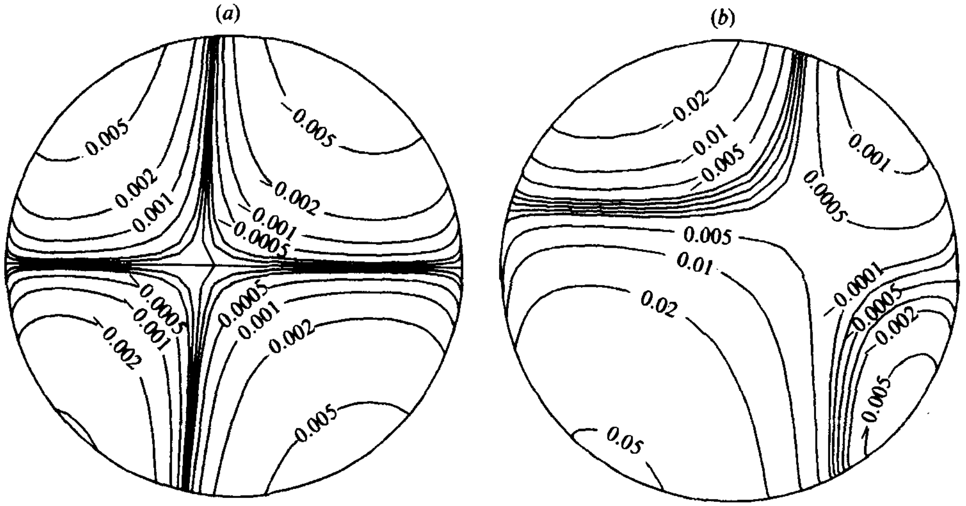

FIGURE 7. Surface contours for $R = 2$ and $\alpha = 0.1$; (*a*) x-component of the pressure; (*b*) total lift force on the particle (viscous contribution + pressure contribution).

and for $\alpha = 0.1$, in figure 6. It can be seen from this figure that, while the total lift is positive – that is, away from the point of zero velocity – for all values of R, the two portions show dramatically different behaviour for different values of the Reynolds number. (All results in figure 6 are for $\alpha = 0.1$.) The viscous contribution is positive and monotonically increasing for all values of Reynolds numbers in the range $0.1 \leqslant R \leqslant 100$, and the dependence of this value upon R is nearly linear at the highest values of R. In contrast, the pressure contribution is positive for $R < 10$, but falls below zero and reaches a minimum at $R \approx 60$. This minimum corresponds to a maximum in downward (i.e. towards the zero velocity direction) force due to pressure. For $R > 60$, up to the highest value of R used here, the pressure contribution monotonically increases.

To understand the behaviour of the pressure contribution, it is necessary to examine the surface distribution of forces on the particle. Plots (*a*) and (*b*) in figures 7, 8 and 9 present the surface contours for the x-component – the vertical component

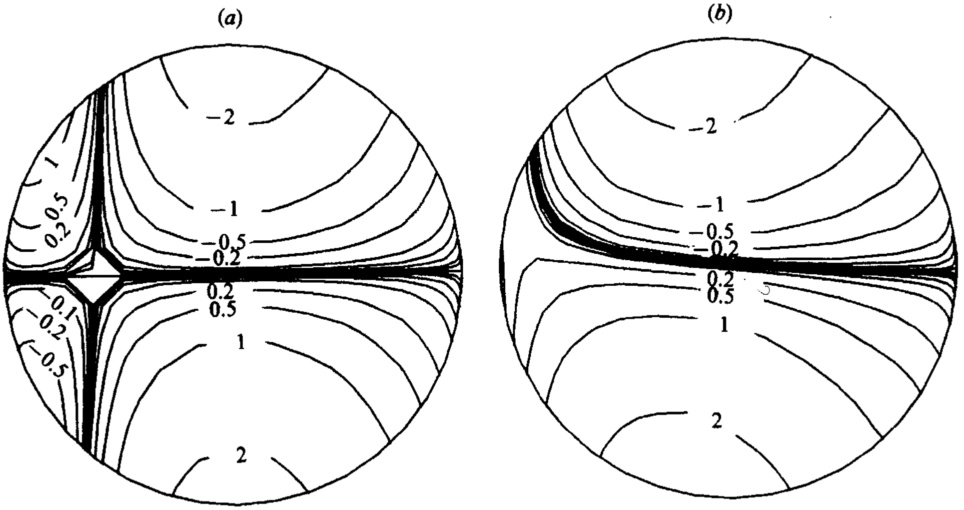

FIGURE 8. Surface contours for $R = 60$ and $\alpha = 0.1$: (*a*) x-component of the pressure; (*b*) total lift force on the particle (viscous contribution + pressure contribution).

in the figures – of the pressure lift contribution (the surface distribution of the contribution from the first term in the expression for F_L) and the total lift (pressure contribution plus viscous contribution), respectively; the three figures correspond to Reynolds numbers of 2, 60, and 100, and $\alpha = 0.1$. For $R = 2$, the flow is nearly fore–aft symmetric, and this is reflected in the rough symmetry in the contours about the midpoint of the particle, $\eta = 0.5$. The upward pressure exerted on the particle for $\zeta < 0.5$ as the flow accelerates to the midpoint ($\eta = 0.5$) offsets the downward force as the fluid decelerates for $\eta < 0.5$. Note that the centre of the particle, $\zeta = 0.5$, must be a zero contour for the x pressure component, because the surface is tangent to the x-direction on this line.

At $R = 60$, figure 8, the flow field is not drastically asymmetric about the line $\zeta = 0.5$, because the difference in velocities between the top and bottom of the particle is only 20%. However, the flow no longer possesses any fore–aft symmetry. It is known (Clift *et al.* 1978) that, for uniform flow at $R = 60$, a closed streamline wake exists on the downstream side of the particle. The presence of this eddy shifts the contours towards the front of the body, and the flow begins to decelerate at a point forward of $\eta = 0.5$. The small region of acceleration and extensive region of deceleration produce a net force on the particle in the downward direction. The flow field will be discussed further in §3.5.

The contours for $R = 100$ are plotted in figure 9. Again, because of the asymmetry of the flow due to the presence of an attached wake, the contours are shifted forward on the particle surface. It can also be seen from figures 7(*a*) and 8(*a*) that the contours do not approach the outflow axis $\eta = 0$ for the $R = 100$ case as they do for the $R = 60$ case. The reason for this difference is that the recirculating wake is larger for $R = 100$ than for $R = 60$, and the point of separation (which depends on ζ) occurs at larger η for $R = 100$ than for the lower Reynolds number. The absence of contour lines in the wake region indicates the weakness of the flow in each eddy.

Although the dimensional lift force increases monotonically with increasing R, the dimensionless lift force, C_L shows different behaviour. Figure 10 indicates the values of C_L corresponding to the lift forces plotted in figure 6. Not shown is the value at

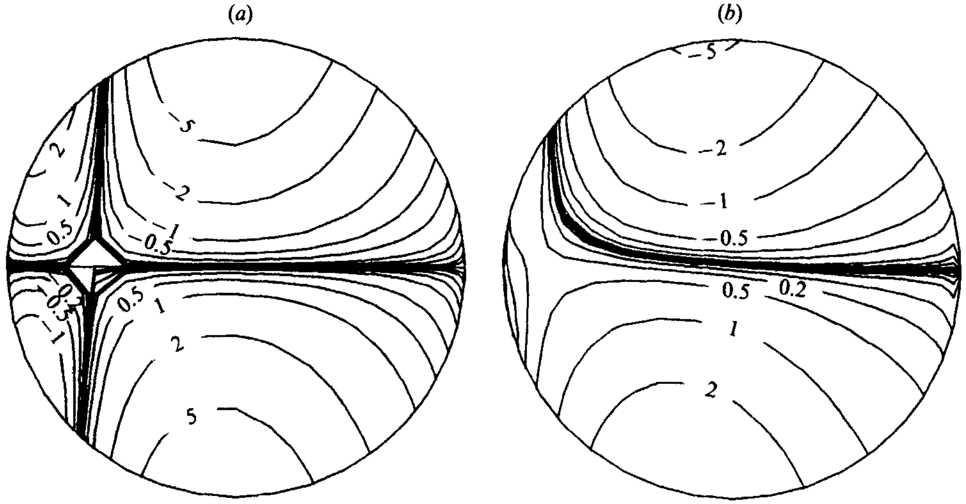

FIGURE 9. Surface contours for $R = 100$ and $\alpha = 0.1$: (a) x-component of the pressure; (b) total lift force on the particle (viscous contribution + pressure contribution).

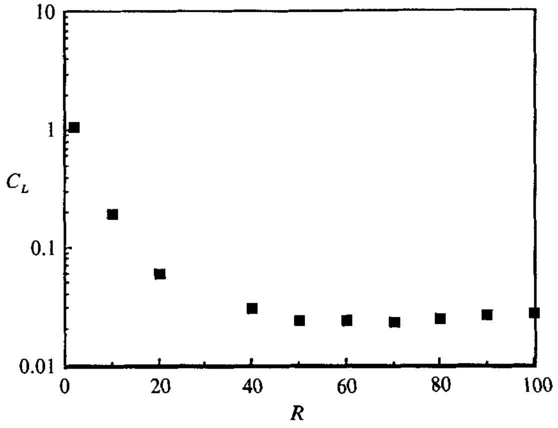

FIGURE 10. Lift coefficient C_L as a function of R for $\alpha = 0.1$.

$R = 0.1$, which is $C_L = 5.72$. The graph in figure 10 can be separated into two regions: in the first, for $R < 40$, the lift coefficient increases sharply with decreasing R, and in the second, for $R > 40$, C_L is essentially independent of the Reynolds number. As demonstrated in figure 3, when the Reynolds number is small enough to apply Saffman's (1965) analysis, the dimensionless lift on the particle increases as $R^{-\frac{1}{2}}$ for fixed α. The invariance of C_L with R for $R > 40$ demonstrates the relative efficiency of lift forces at modest Reynolds numbers. In other words, increases in the inertia of the flow (ρU_∞^2) are accompanied by a linear increase in the amount of lift imparted to the particle, whereas at lower values of R, where viscous effects dominate, the lift coefficient is roughly proportional to the inverse of the square root of the Reynolds number; thus, the dimensional lift is proportional to $U_\infty^{\frac{3}{2}}$. Quite similar qualitative behaviour is observed for the cases $\alpha = 0.2$ and $\alpha = 0.4$, but the value of the Reynolds number where C_L levels off increases slightly with α.

To examine the effect of the shear rate α on the lift at moderate Reynolds numbers, a calculation was done at $R = 40$. Figure 11 (a) presents the lift coefficient at $R = 40$

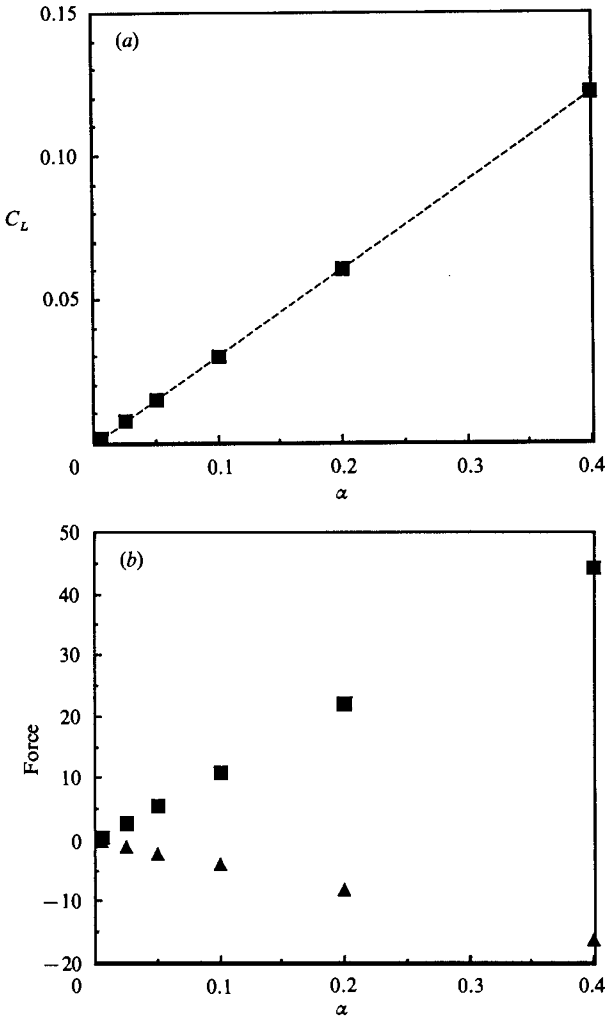

FIGURE 11. (*a*) Lift coefficient C_L as functions of α for $R = 40$. (*b*) Dimensional pressure (▲) and viscous (■) contributions to the lift force as a function of α for $R = 40$.

for six values of α: 0.005, 0.025, 0.05, 0.1, 0.2, and 0.4. The dashed line has been added to demonstrate the linear proportionality between C_L and α. The fact that $C_L \propto \alpha$ at an intermediate value of R is somewhat surprising since $C_L \propto \alpha^{\frac{1}{2}}$ at very small values of R. The pressure and viscous contributions of the dimensional lift force for these six values of α are plotted in figure 11(*b*). Both of the force terms double in magnitude as α doubles, but the pressure portion is negative. Since both double in magnitude as α doubles for this value of R, the relative contributions of viscous lift and pressure lift remain constant.

3.3. *Drag*

The drag coefficients C_D for $\alpha = 0.1$, 0.2, and 0.4, and Reynolds numbers in the range $1 \leqslant R \leqslant 100$ are plotted in figure 12. Here, the square symbols correspond to the solutions for $\alpha = 0.1$, the triangles to $\alpha = 0.2$, and the circles to $\alpha = 0.4$. These values for the drag coefficient closely parallel the behaviour of drag for steady uniform flow past a spherical particle ($\alpha = 0$), as plotted in figure 13 for $\alpha = 0.1$. In figure 13 the

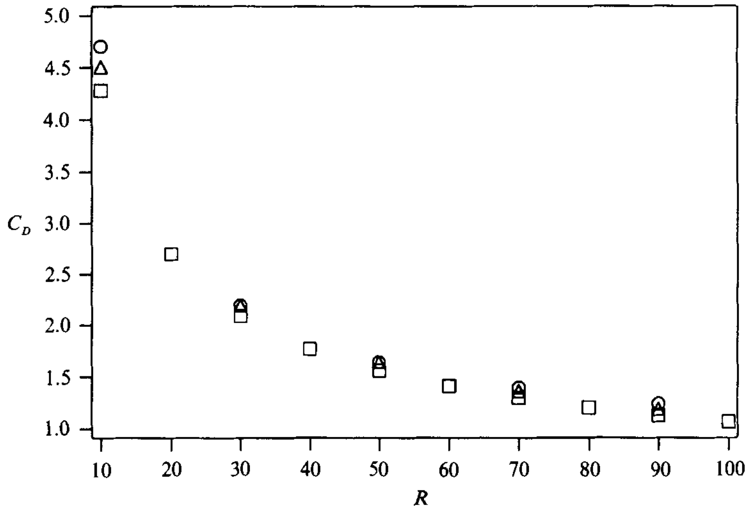

FIGURE 12. The drag coefficient C_D as a function of R for $\alpha = 0.1$ (□), 0.2 (△), and 0.4 (○).

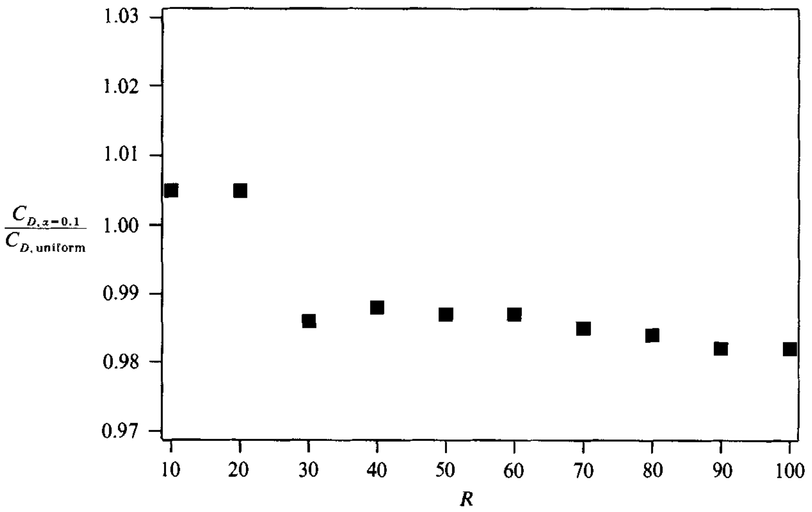

FIGURE 13. The ratio of drag coefficients computed in this work ($\alpha = 0.1$) to drag coefficients computed using the correlations of Clift *et al.* (1978) for uniform flow.

numerical solutions computed in this work for $\alpha = 0.1$ have been normalized using the drag correlations for steady uniform flow found in Clift *et al.* (1978). For Reynolds numbers above 20, $C_D(\alpha = 0.1) \approx 0.98 C_D(\alpha = 0)$, with this proportionality valid up to the highest values of R studied. For the $\alpha = 0.2$ case, the proportionality is 0.99, and for $\alpha = 0.4$ it is nearly unity. It is interesting to note that, for a fixed shear rate, the z-component of the force on the particle is a constant fraction of the force the particle undergoes in uniform flow, and is independent of the Reynolds number. The explanation for this behaviour is that for fixed α the difference in velocity between the bottom and the top of the particle is constant relative to the midpoint velocity. This constant relative velocity change across the particle yields a pseudo-mean velocity which is a constant fraction of the centreline velocity.

The surface contours of the two contributions to drag are presented in plots (a) and

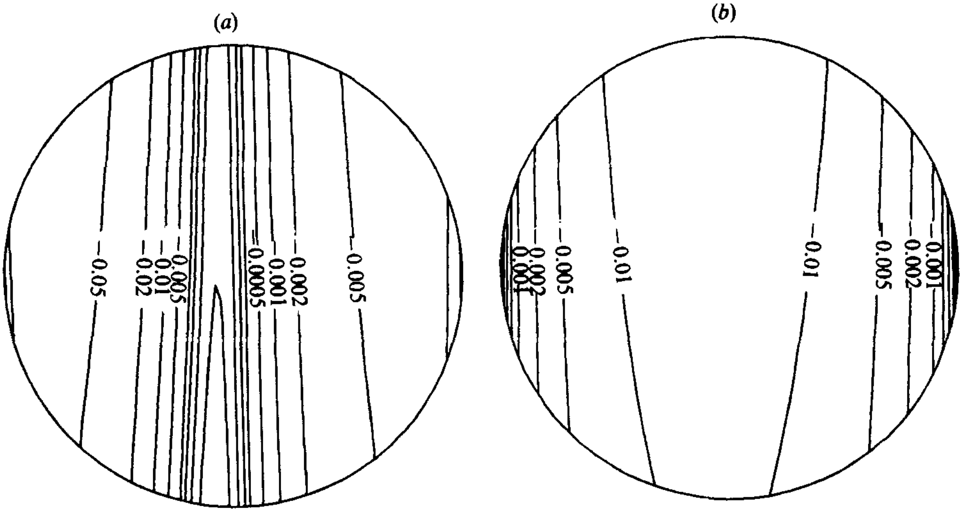

FIGURE 14. Surface contours for $R = 2$ and $\alpha = 0.1$: (*a*) z-component of the pressure; (*b*) z-component of the viscous stress.

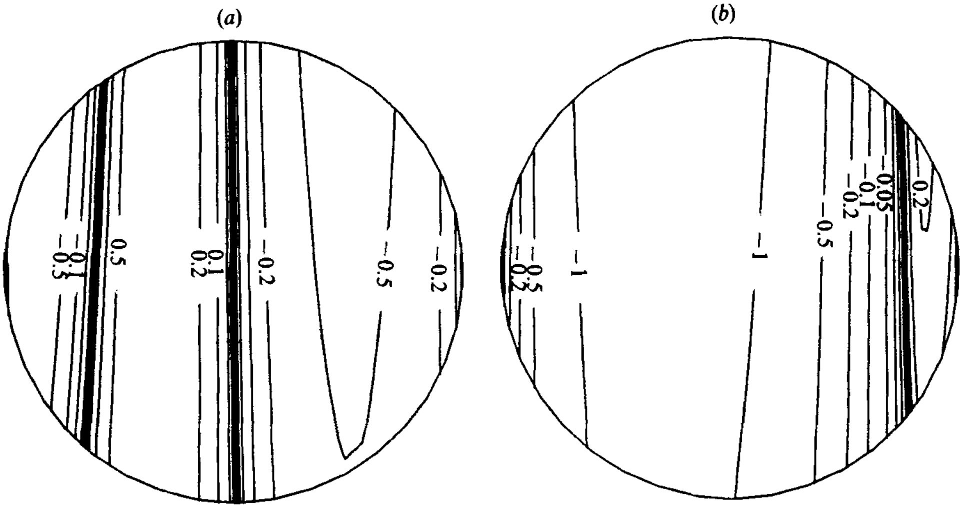

FIGURE 15. Surface contours for $R = 60$ and $\alpha = 0$: (*a*) z-component of the pressure; (*b*) z-component of the viscous stress.

(*b*) of figures 14–16 for $\alpha = 0.1$ and Reynolds numbers of 2, 60 and 100. As with the x-components of force, the contours in figure 14 for $R = 2$ are nearly symmetric about the line $\eta = 0.5$. The viscous contribution reaches a maximum at the top of the particle ($\zeta = 0$), in the region of highest velocities, where the surface is tangent to the z-direction. The pressure force goes to zero on the line $\eta = 0.5$, since the surface is everywhere tangent to the z-direction on this line.

Figures 15(*a*) and 15(*b*) show that the force contours are shifted forward slightly owing to the asymmetry of the flow around the particle and the presence of a recirculating wake, but this asymmetry is not too extreme at this value of R. The maximum in the viscous contribution lies near $(\eta, \zeta) = (0.5, 0)$, since the velocity maximum is not too far forward of this point, and the surface is nearly parallel to the

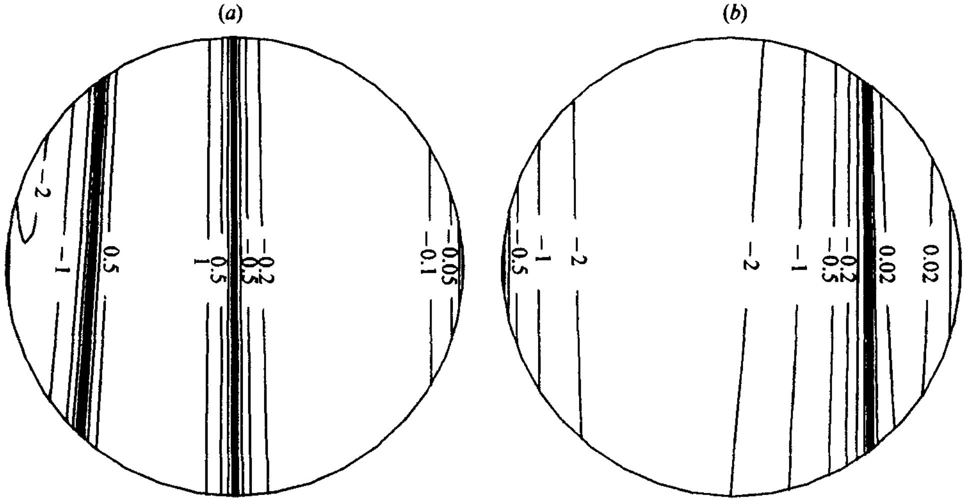

FIGURE 16. Surface contours for $R = 100$ and $\alpha = 0.1$: (a) z-component of the pressure: (b) z-component of the viscous stress.

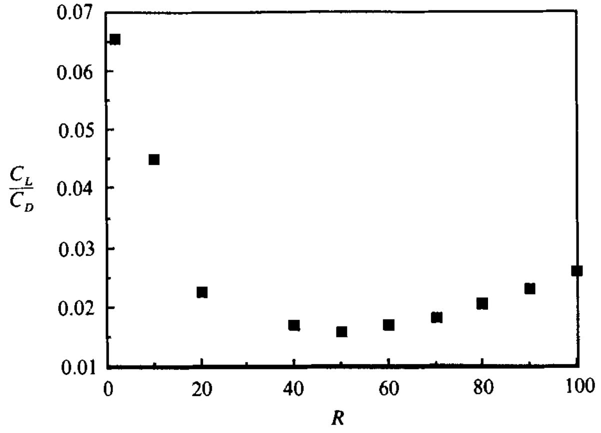

FIGURE 17. The ratio of lift to drag (C_L/C_D) as a function of R at $\alpha = 0.1$.

z-direction. Owing to the geometry of the system the pressure must be distributed about the line $\eta = 0.5$, and as a consequence the concentration of contours becomes noticeably higher in the front than the back.

At a Reynolds number of 100 (figure 16), the pressure contours are at a significantly higher density in the front than in the back, owing in large part to the large stagnation pressure at the front of the particle, and the existence of separated flow at the rear of the body. The location of the largest viscous contribution is shifted slightly more forward than for the $R = 60$ case. This invarience is typical for intermediate Reynolds number flows: once modest values of R are reached and inertial effects become important, the shape (or, distribution) of the flow field on the upstream side of the particle is rather insensitive to changes in R, whereas the structure of the flow field on the downstream side can change dramatically. Therefore, the position and structure of the contour distribution for $\eta > 0.5$ (the upstream side) should not be strongly dependent on the value of the Reynolds number.

The relative magnitudes of lift and drag are plotted in figure 17 for a fixed value of $\alpha = 0.1$. At lower values of the Reynolds number, particularly for $R < 10$, the lift-to-drag ratio increases sharply as R decreases, but the magnitude of the ratio is still small at this shear rate. The ratio C_L/C_D decreases monotonically up to $R \approx 50$, which, not coincidentally, is near the point where the pressure contribution to the lift force reaches a minimum. Above this Reynolds number, the pressure portion of the lift force increases, and the lift-to-drag ratio also increases monotonically up to the highest value of R.

3.4. *Heat transfer*

Theoretical studies of the relationship between the Nusselt or Sherwood number and the Péclet number for spheres date back to the work of Acrivos & Taylor (1962), who used Stokes solution for the velocity field around a sphere in a matched asymptotic solution of the thermal energy equation. This work was extended by Rimmer (1968) using the velocity field due to Proudman & Pearson (1957) to account for small but non-zero values of R.

These results apply only in the limit of small Reynolds number, and other researchers, employing experimental or numerical techniques, have examined correlations for heat and mass transfer at intermediate values of R. Ranz & Marshall (1952*a*, *b*) proposed the following correlation:

$$Nu = 2+0.60R^{\frac{1}{2}}P^{\frac{1}{3}}.$$

Later, Beard & Pruppacher (1971) performed a series of wind-tunnel experiments to study the rate of evaporation of water drops. Woo & Hamielec (1971), in conjunction with the experiments of Beard & Pruppacher (1971), carried out a series of numerical calculations to theoretically predict the same phenomena. The heat transfer analogue of the correlation presented by Beard & Pruppacher is

$$Nu = 1.56+0.616R^{\frac{1}{2}}P^{\frac{1}{3}},$$

and the numerical results of Woo & Hamielec (1971) agree with this correlation ($\pm 2\%$) over the entire range of R considered. Beard & Pruppacher's result converges to the theoretical predictions of Acrivos & Taylor (1962) for small Reynolds numbers. However, the correlation of Ranz & Marshall consistently predicts higher rates of heat transfer than does that due to Beard & Pruppacher, and the difference is 16% at the smallest values of R considered. Beard & Pruppacher attribute the discrepancy between their correlation and the Ranz & Marshall correlation to a number of experimental defects in the Ranz & Marshall study.

Another correlation of Nu is due to Whitaker (1972), who found that the best fit of experimental data was

$$Nu = 2+(0.4R^{\frac{1}{2}}+0.06R^{\frac{2}{3}})P^{0.4}.$$

The two different Reynolds-number dependencies are intended to take into account differences in the magnitude in heat transfer between a forward boundary-layer region and a rear wake region. Sayegh & Gauvin (1979) used numerical techniques to predict that for constant fluid properties

$$Nu = 2+0.473R^{0.552}P^{m},$$

where $m = 0.78/R^{0.145}$. Sayegh & Gauvin found that their result agreed closely with that of Beard & Pruppacher (1971), but the correlation of Ranz & Marshall (1952*a*, *b*) consistently over-predicted Nu at low Reynolds numbers. However, the correlations of Ranz & Marshall and Sayegh & Gauvin converge as $R \rightarrow 100$. The

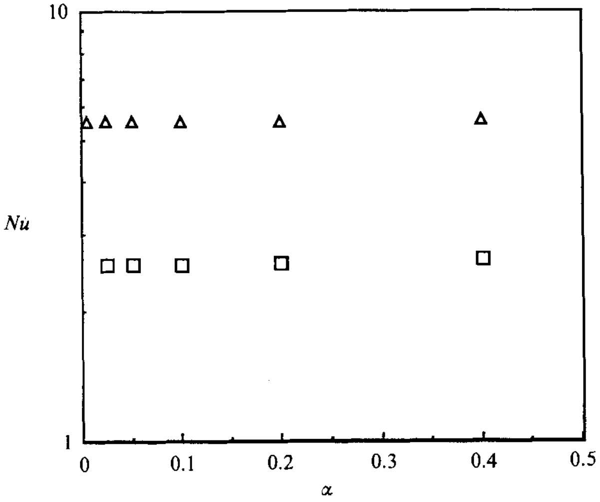

FIGURE 18. The dimensionless rate of heat transfer, Nu, as a function of α for $R = 1$ (□) and $R = 40$ (△).

result of Whitaker (1972) is fairly close to that of Sayegh & Gauvin for $R < 10$, but above this value the two correlations diverge.

To examine the effect of suction or injection on the heat transfer rate to a sphere, Chuchottaworn (1984) performed a numerical study for a wide range of Reynolds numbers and blowing rates. Chuchottaworn found that in the absence of suction or injection,

$$Nu = 2+0.37R^{0.61}P^{0.51}.$$

For the range of values of the parameter α studied here ($0.005 \leqslant \alpha \leqslant 0.4$), it was found that, while the rate of heat transfer to the particle surface increased monotonically with increasing Reynolds number, the heat transfer rate was relatively insensitive to the value of α at fixed R, as demonstrated in figure 18. The dimensionless rate of heat transfer, Nu (see (8)), is plotted as a function of α for two different Reynolds numbers, $R = 1$ and $R = 40$. As expected, the rate of heat transfer is higher for $R = 40$ than for $R = 1$, but, surprisingly, Nu is essentially independent of α. These results indicate that although the surface distribution of heat flux changes with α, in an integral sense the average temperature gradient at the particle surface depends only on the Reynolds number, that is, on the value of the centreline velocity U_∞. It was found at other values of R ($R = 2$, 10, and 100) that $Nu(\alpha = 0) = Nu(\alpha = 0.1)$, and the values of Nu at $\alpha = 0.4$ only deviate from the values at $\alpha = 0$ by 2% at most.

Since the Nusselt number is independent of α in the results found here, a comparison is made between the numerical results obtained for Nu in this work with those computed using the correlations valid for uniform flow past a spherical particle, listed above. The Nusselt number Nu is plotted as a function of R, (for $P = 1$) in figure 19. The closed symbols denote the results from this work, and the curves are from the correlations of Ranz & Marshall (1952*a*, *b*), Beard & Pruppacher (1971), Whitaker (1972) and Sayegh & Gauvin (1979). Over the range of Reynolds numbers studied in this work ($0.1 \leqslant R \leqslant 100$), we find that our results for heat transfer are in closest agreement with the correlation of Whitaker (1972). The Ranz & Marshall correlation predicts larger values of Nu than do our numerical results for all R

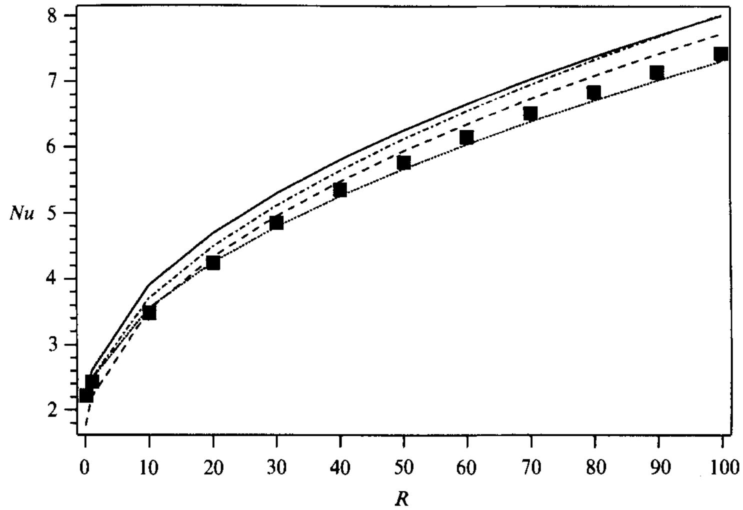

FIGURE 19. The dimensionless rate of heat transfer, Nu as a function of R for values computed in this work (symbols) and using the correlations of Ranz & Marshall (1952*a, b*) (——); Beard & Prupacher (1971) (– – –); Whitaker (1972) (······), Sayegh & Gauvin (1979) (- - - -).

considered, as does the correlation of Sayegh & Gauvin. Our results are very close to the predictions of Beard and Pruppacher for $R < 40$, but for larger values of R their correlation yields higher heat transfer rates.

3.5. *The flow field*

For a spherical particle in uniform flow – corresponding to $\alpha = 0$ here – it is recognized that at a Reynolds number of approximately 20 flow separation occurs at a line on the sphere surface forward of the rear stagnation point (Rimon & Cheng 1969; Taneda 1956). Since the flow is axisymmetric, the separation line inscribes a circular arc, that is, the point of separation on the surface is independent of the azimuthal position. Further, it is generally agreed that flow separates at, or very near, the point where the streamwise component of the surface shear vanishes (Brown & Stewartson 1969; Williams 1977), or equivalently, the point where the surface vorticity changes sign. Thus, in two-dimensional and axisymmetric flows, one looks for flow separation by examining the magnitude of surface shear or vorticity. However, for a fully developed three-dimensional flow, there are two orthogonal components of the surface shear stress, and if we extrapolate from the condition for two-dimensional flow separation, then in order for flow separation to occur in three dimensions, *both* components of the surface shear must simultaneously vanish. However, it is not reasonable to assume that this criterion will be met, except at isolated points on the body surface and, as will be shown below, three-dimensional flow separation does indeed exist without having both components of the shear stress vanish.

A detailed examination of three-dimensional flow separation, and the relationships between separation and surface shear stress will be presented elsewhere; here we shall present a single case in order to elucidate the curious nature of three-dimensional separation. Consider the case $R = 70$. As mentioned above, at this value of R a closed-streamline wake will exist behind the sphere for uniform flow, $\alpha = 0$. To examine the effect of the three-dimensional nature of the shear flow studied here on separation, we look at the flow field, components of the surface shear stress, and surface pressure,

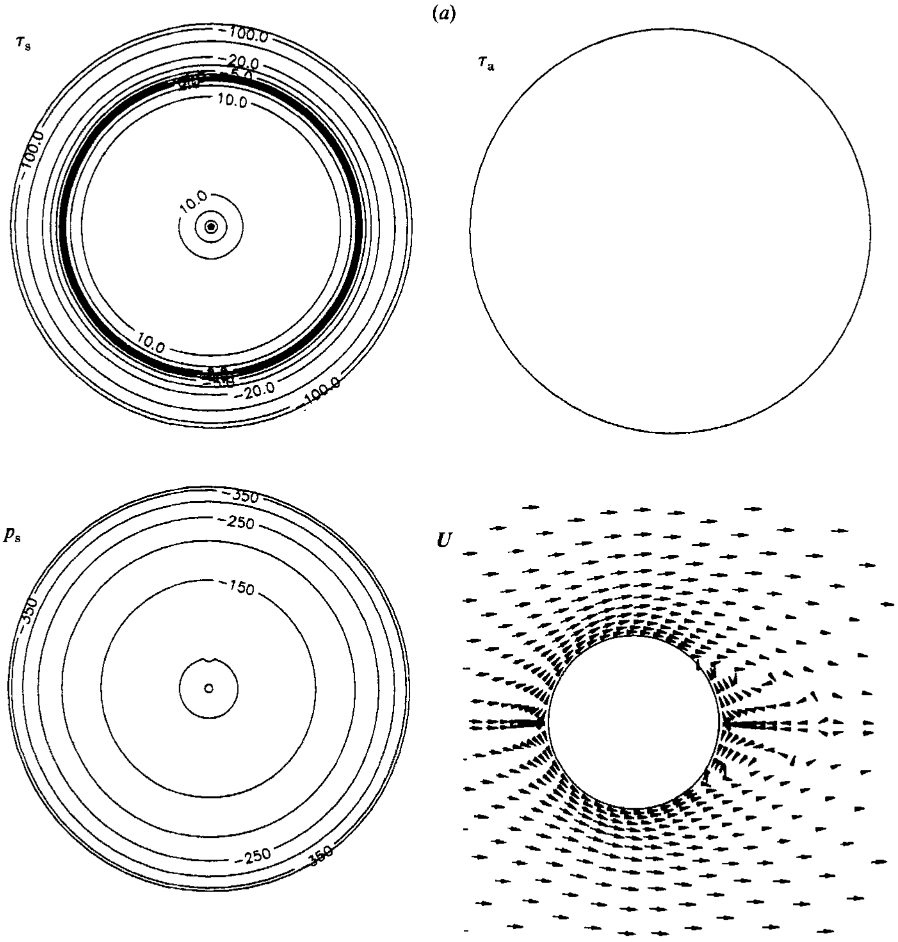

FIGURE 20(a). For caption see page 406.

for $\alpha = 0$, 0.2, and 0.4. In figure 20(a–c) we have plotted the velocity field in the symmetry plane as viewed from an orientation normal to the plane of the undisturbed shear flow; contours of the streamwise component of the surface shear stress, τ_s; contours of the azimuthal component of surface shear stress, τ_a; and contours of the surface pressure, p_s. The three contour plots in each of figures 20(a)–(c) are shown as viewed from the rear of the sphere, looking along the positive z-axis back towards the origin. In figure 20(a) ($\alpha = 0$) we see that the contours of the streamwise component of surface shear form concentric circles, proving that the flow is axisymmetric, and thus independent of ζ. It then follows that the azimuthal component is everywhere zero, and the pressure contours also form concentric circles. The position on the surface where τ_s changes sign is computed to be 47.5° from the rear stagnation point and, as pointed out earlier in table 1, this agrees well with other published results. The length of the wake in the velocity plot is determined by examining the z-component of the velocity field along the line $\eta = 0$. The measured wake length also agrees closely with published results (table 1).

For the case $\alpha = 0.2$, figure 20(b), the stress and pressure contours exhibit significant asymmetric behaviour. This asymmetry is evident in the contours for τ_s

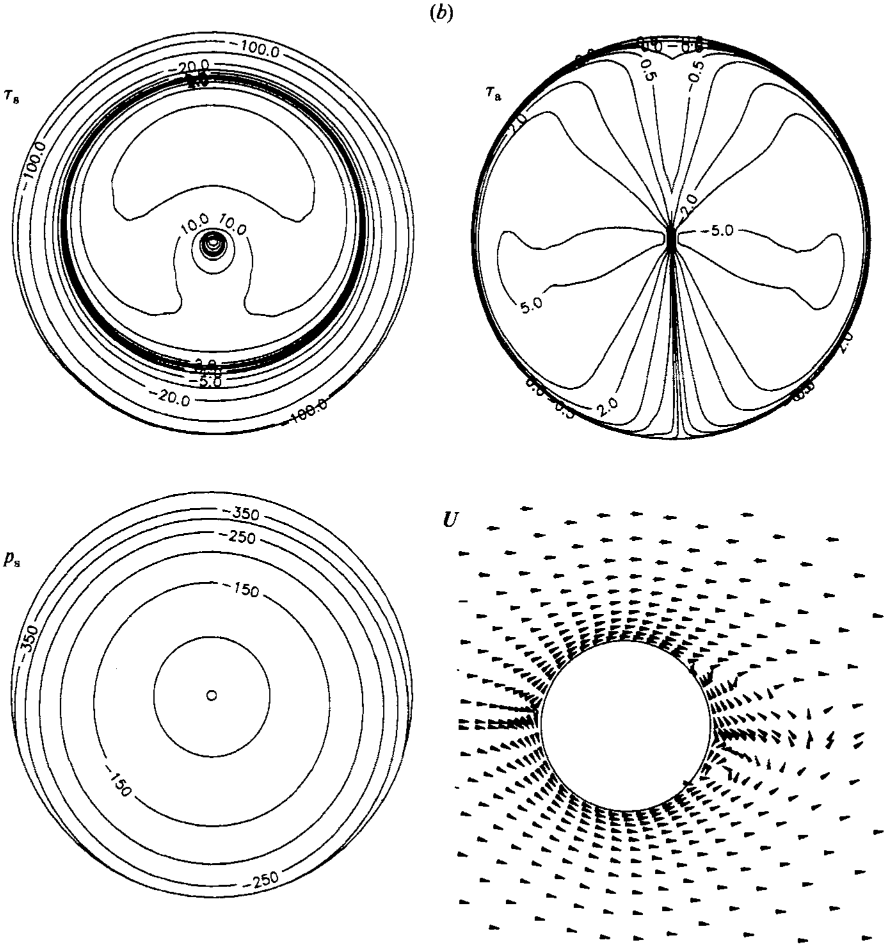

FIGURE 20(*b*). For caption see page 406.

and p_s in figure 20(*b*). Because of the asymmetry, the arc of vanishing τ_s is no longer perfectly circular, as with the $\alpha = 0$ case. Now, points lying on a vertical line drawn through the centre point of the τ_s contours correspond to points on back side of the sphere surface shown in the plot of the velocity field. In other words, the vertical line bisecting the contour plot corresponds to the semicircular arc denoting the sphere surface in the symmetry plane, the curve $x^2+z^2 = 1$, $z > 0$. Using arguments pertinent to two-dimensional flow separation, it is reasonable to state that the two points of vanishing τ_s lying on the vertical line correspond to the two points of flow separation shown in the plot of the velocity field in figure 20(*b*). The reasoning is as follows. The two relevant components of the stress tensor, written in the general curvilinear components, are

$$\tau_{\xi\eta} = \frac{1}{h_\xi}\left[\frac{\partial u_\eta}{\partial \xi} - \frac{u_\xi}{h_\eta}\frac{\partial h_\xi}{\partial \eta}\right] + \frac{1}{h_\eta}\left[\frac{\partial u_\xi}{\partial \eta} - \frac{u_\eta}{h_\xi}\frac{\partial h_\eta}{\partial \xi}\right], \tag{13a}$$

$$\tau_{\xi\zeta} = \frac{1}{h_\xi}\left[\frac{\partial u_\zeta}{\partial \xi} - \frac{u_\xi}{h_\zeta}\frac{\partial h_\xi}{\partial \zeta}\right] + \frac{1}{h_\zeta}\left[\frac{\partial u_\xi}{\partial \zeta} - \frac{u_\zeta}{h_\xi}\frac{\partial h_\xi}{\partial \xi}\right], \tag{13b}$$

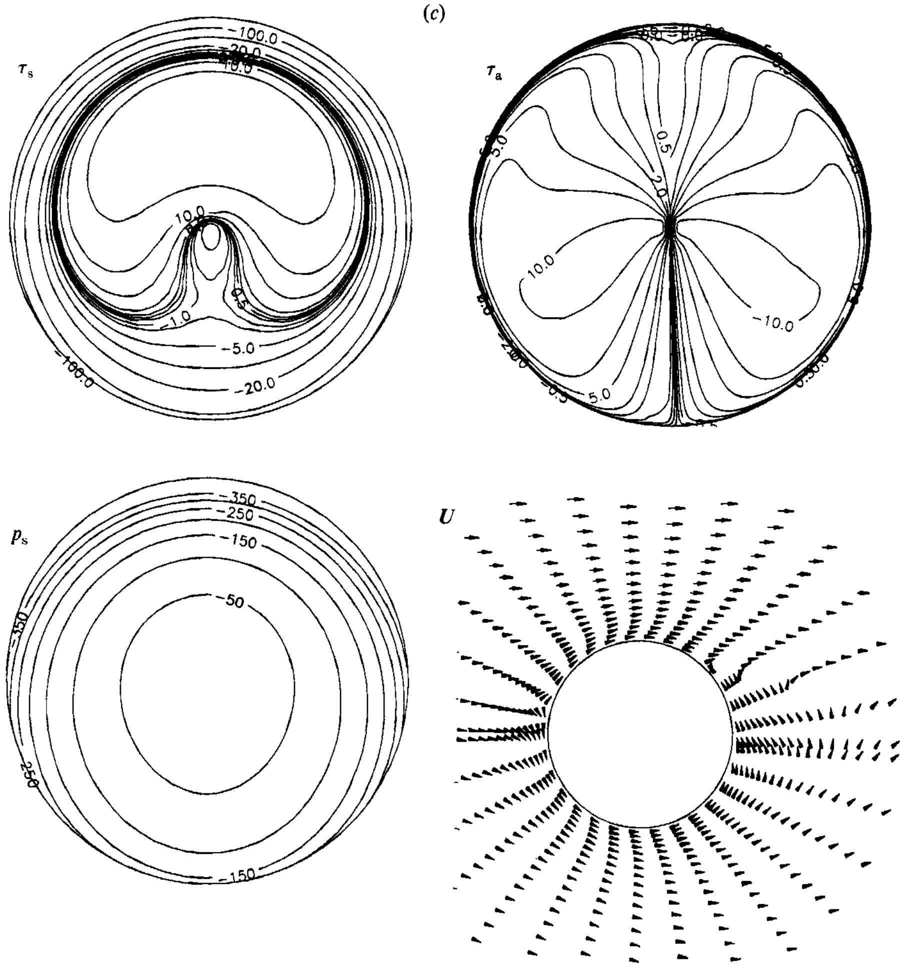

FIGURE 20. Plots displaying the velocity field in the symmetry plane, and contours of the two components of the surface shear stress and surface pressure on the rear half of the sphere at $R = 70$ and (a) $\alpha = 0$, (b) $\alpha = 0.2$, and (c) $\alpha = 0.4$.

where h_ξ^2, h_η^2, and h_ζ^2 are the three diagonal components of the metric tensor, and u_ξ, u_η, and u_ζ are the curvilinear components of the velocity vector. When (13*a*) and (13*b*) are evaluated at the sphere surface ($\xi = 0$), we obtain

$$\tau_s = \tau_{\xi\eta}\Big|_{\xi=0} = \frac{1}{h_\xi}\frac{\partial u_\eta}{\partial \xi}\Big|_{\xi=0}, \tag{14a}$$

$$\tau_a = \tau_{\xi\zeta}\Big|_{\xi=0} = \frac{1}{h_\xi}\frac{\partial u_\zeta}{\partial \xi}\Big|_{\xi=0}. \tag{14b}$$

Therefore, in the symmetry plane $y = 0$ the azimuthal component, τ_a, is identically zero, as demonstrated in the contours for τ_a, and it is logical that separation will occur when the other component of stress, τ_s vanishes. This supposition is born out by comparing the points where τ_s vanishes on the arc in the symmetry plane with the sign of u_η at the grid points nearest the sphere surface. The results indicate a separation point on the high-velocity surface located 50° from the boundary $\eta = 0$ (the positive z-axis), and at a point on the low-velocity surface located 42° from $\eta = 0$. The connection between separation and the magnitudes of τ^{s} and τ_{a} at points on the surface outside of the symmetry plane are, at this time, not fully understood. It is tempting to state that for the flows studied here, separation is directly related to the magnitude of τ_{s}, but this would be premature and unsupportable.

The most startling feature of figure 20(*b*) is the flow field itself. First, the forward stagnation point is no longer located at $(\xi, \eta) = (0, 1)$; it has been shifted upward on the high-velocity side of the sphere surface by a few degrees. Also, a closed-streamline wake exists on the lower surface at the rear, just as for $\alpha = 0$, but the recirulating eddy on the upper portion of the sphere has disappeared, even though there still exists a separation point located 50° from $\eta = 0$. Fluid moving around the bottom of the sphere continues *around* the recirculating wake, and up the back of the sphere until departing at the separation point. This startling result could not have been predicted simply by examining the contours for τ_{s} or τ_{a}.

Finally, for the $\alpha = 0.4$ case, shown in figure 20(*c*), we see that the asymmetry in the contours is greatest. The τ_{s} contours show that there is no point on the lower surface of the sphere in the symmetry plane where the streamwise component of shear vanishes. The velocity field in the symmetry plane emphasizes the unusual shape of the τ_{s} contours. The low eddy, appearing for $\alpha \leqslant 0.2$, has disappeared, and there is now only one separation point in this plane. Fluid elements moving around the top of the sphere meet elements that have travelled all the way around the bottom and up the back of the sphere. The flow separates from the surface in this plane at an angle of 53° measured from the $\eta = 0$ boundary, and this point coincides with the point where τ_{s} vanishes. Because the velocity of the undisturbed flow goes to zero at a distance of 2.5 radii from the sphere centre, two regions of flow reversal exist below the sphere. It is interesting that, as α is increased, the locations of the forward stagnation point and the rear separation point move closer to one another.

4. Conclusion

Numerical solutions have been obtained for steady, linear shear flow past a non-translating, non-rotating spherical particle. This flow problem is fully three-dimensional, and a powerful finite-volume technique has been employed to solve the full Navier–Stokes equations and the thermal energy equation. A wide range of flow parameters has been investigated ($0.1 \leqslant R \leqslant 100$, $0.005 \leqslant \alpha \leqslant 0.4$) and the validity of the solutions for the entire parameter space has been demonstrated from the accuracy tests.

The dimensional lift force on the particle, F_L, is observed to increase monotonically with both the Reynolds number and the shear rate, but the dimensionless lift coefficient, C_L, is approximately constant for fixed α for Reynolds numbers in the range $40 \leqslant R \leqslant 100$. The insensitivity of C_L to the Reynolds number indicates that the lift on the particle increases in direct proportion to the inertia of the flow. At lower values of the Reynolds number ($R < 10$), it was seen that $C_L \propto R^{-\frac{1}{2}}$.

The dimensional drag force on the particle, F_D, also increases with both R and α, but C_D decreases monotonically with increasing R for fixed α. Further, for fixed α, the drag coefficient, normalized by the drag coefficient for uniform flow, is constant for Reynolds numbers in the range $40 \leqslant R \leqslant 100$. Therefore, the drag on a particle at specified values of $\tilde{\alpha}$ and U_∞ is a constant fraction of the drag on a particle in uniform flow at the same centreline velocity.

For the range of shear rates studied in this work, the rate of heat transfer to the particle surface is insensitive to the value of α, suggesting that the average temperature gradient at the particle surface depends, to lowest order, on the centreline velocity U_∞. The dimensionless heat transfer rate Nu (the Nusselt number) rises monotonically with increasing R, with the dependence on the Reynolds number decreasing with R; that is, the slope of the curve described by plotting Nu versus R decreases as R increases.

The nature of three-dimensional flow separation is very complex, and the relationships between separation and shear stress are not yet fully understood. Future work will yield a greater understanding of this phenomena.

This work was partially supported by the US Department of Energy, Office of Basic Energy Sciences, Division of Engineering and Geosciences; and partially supported by a Memorandum of Understanding between the US Department of Energy and the US Army.

The large scale of the computations done in this work necessitated the utilization of the large-memory capabilities of the CRAY-2 located at the Ballistics Research Laboratory, Aberdeen, Maryland. The authors gratefully acknowledge the use of these computing facilities, and thank George Adams at BRL for his assistance.

The authors would like to thank one of the referees for the large amount of time put into the review, and for the many constructive suggestions.

REFERENCES

ACRIVOS, A. & TAYLOR, T. D. 1962 Heat and mass transfer from single spheres in Stokes flow. *Phys. Fluids* **5**, 387–394.

BEARD, K. V. & PRUPPACHER, H. R. 1971 A wind tunnel investigation of the rate of evaporation of small water drops falling at terminal velocity in air. *J. Atmos. Sci.* **28**, 1455–1464.

BRABSTON, D. C. & KELLER, H. B. 1975 Viscous flows past spherical gas bubbles. *J. Fluid Mech.* **69**, 179–189.

BRETHERTON, F. P. 1962 The motion of rigid particles in a shear flow at low Reynolds number. *J. Fluid Mech.* **14**, 284–304.

BRIGNELL, A. S. 1973 The deformation of a liquid drop at small Reynolds number. *Q. J. Mech. Appl. Maths* **26**, 99–107.

BROWN, S. N. & STEWARTSON, K. 1969 Laminar separation. *Ann. Rev. Fluid Mech.* **1**, 45–72.

CHORIN, A. J. 1967 A numerical method for solving incompressible viscous flow problems. *J. Comput. Phys.* **2**, 12–26.

CHORIN, A. J. 1968 Numerical solution of incompressible flow problems. *Studies in Numerical Analysis 2*, pp. 64–70. Philadelphia: SIAM.

CHRISTOV, C. I. & VOLKOV, P. K. 1985 Numerical investigation of the steady viscous flow past a stationary deformable bubble. *J. Fluid Mech.* **158**, 341–364.

CHUCHOTTAWORN, T. 1984 Numerical analysis of heat and mass transfer from a sphere with surface mass injection or suction. *J. Chem. Engng Japan* **17**, 1–7.

CLIFT, R., GRACE, J. R. & WEBER, M. E. 1978 *Bubbles, Drops, and Particles*. Academic.

COX, R. G. & BRENNER, H. 1968 The lateral migration of solid particles in Poiseuille flow – I. *Theory*. *Chem. Engng Sci.* **23**, 147–173.

DANDY, D. S. & LEAL, L. G. 1989 Buoyancy-driven motion of a deformable drop through a quiescent liquid at intermediate Reynolds numbers. *J. Fluid Mech.* **208**, 161–192.

DWYER, H. A. 1989 Calculations of droplet dynamics in high temperature environments. *Prog. Energy Combust. Sci.* **15**, 131–158.

FORNBERG, B. 1988 Steady viscous flow past a sphere at high Reynolds numbers. *J. Fluid Mech.* **190**, 471–489.

Harper, J. F. 1972 The motion of bubbles and drops through liquids. *Adv. Appl. Mech.* **12**, 59–129.

Harper, J. F. & Moore, D. W. 1968 The motion of a spherical liquid drop at high Reynolds number. *J. Fluid Mech.* **32**, 367–391.

Ho, B. P. & Leal, L. G. 1974 Intertial migration of rigid spheres in two-dimensional unidirectional flows. *J. Fluid Mech.* **65**, 365–400.

LeClair, B. P., Hamielec, A. E., Pruppacher, H. R. & Hall, W. D. 1972 A theoretical and experimental study of the internal circulation in water drops falling at terminal velocity in air. *J. Atmos. Sci.* **29**, 728–740.

Masliyah, J. H. 1970 Symmetric flow past orthotropic bodies: single and clusters. Ph.D. thesis, University of British Columbia, Vancouver.

Moore, D. W. 1959 The rise of a gas bubble in a viscous liquid. *J. Fluid Mech.* **6**, 113–130.

Moore, D. W. 1963 The boundary layer on a spherical gas bubble. *J. Fluid Mech.* **16**, 161–176.

Moore, D. W. 1965 The velocity of rise of distorted gas bubbles in a liquid of small viscosity. *J. Fluid Mech.* **23**, 749–766.

Oliver, D. L. R. & Chung, J. N. 1987 Flow about a fluid sphere at low to moderate Reynolds numbers. *J. Fluid Mech.* **177**, 1–18.

O'Neill, M. E. 1968 A sphere in contact with a plane wall in a slow linear shear flow. *Chem. Engng Sci.* **23**, 1293–1298.

Peacemann, D. W. & Rachford, H. H. 1955 The numerical solution of parabolic and elliptic differential equations. *J. Soc. Indust. Appl. Maths* **3**, 28–41.

Proudman, I. & Pearson, J. R. A. 1957 Expansions at small Reynolds numbers for the flow past a sphere and a circular cylinder. *J. Fluid Mech.* **2**, 237–262.

Ranz, W. E. & Marshall, W. R. 1952*a* Evaporation from drops: Part I. *Chem. Engng Prog.* **48**, 141–146.

Ranz, W. E. & Marshall, W. R. 1952*b* Evaporation from drops: Part II. *Chem. Engng Prog.* **48**, 173–180.

Rimmer, P. L. 1968 Heat transfer from a sphere in a stream of small Reynolds number. *J. Fluid Mech.* **32**, 1–19.

Rimon, Y. & Cheng, S. I. 1969 Numerical solution of a uniform flow over a sphere at intermediate Reynolds numbers. *Phys. Fluids* **12**, 949–959.

Rivkind, V. Y. & Ryskin, G. 1976 Flow structure in motion of a spherical drop in a fluid medium at intermediate Reynolds numbers. *Fluid Dyn.* **11**, 5–12.

Roache, P. J. 1972 *Computational Fluid Dynamics*. Albuquerque: Hermosa.

Rubinow, S. I. & Keller, J. B. 1961 The transverse force on a spinning sphere moving in a viscous fluid. *J. Fluid Mech.* **11**, 447–459.

Ryskin, G. & Leal, L. G. 1984*a* Large deformations of a bubble in axisymmetric steady flows. Part 1. Numerical techniques. *J. Fluid Mech.* **148**, 1–17.

Ryskin, G. & Leal, L. G. 1984*b* Large deformations of a bubble in axisymmetric steady flows. Part 2. The rising bubble. *J. Fluid Mech.* **148**, 19–35.

Saffman, P. G. 1965 The lift on a small sphere in a slow shear flow. *J. Fluid Mech.* **22**, 385–400, and Corrigendum. *J. Fluid Mech.* **31** (1968), 624.

Sayegh, N. N. & Gauvin, W. H. 1979 Numerical analysis of variable property heat transfer to a single sphere in high-temperature surroundings. *AIChE J.* **25**, 522–534.

Schonberg, J. A., Drew, D. A. & Belfort, G. 1986 Viscous interactions of many neutrally buoyant spheres in Poiseuille flow. *J. Fluid Mech.* **167**, 415–426.

Schonberg, J. A. & Hinch, E. J. 1989 Inertial migration of a sphere in Poiseuille flow. *J. Fluid Mech.* **203**, 517–524.

Taneda, S. 1956 Experimental investigation of the wake behind a sphere at low Reynolds numbers. *J. Phys. Soc. Japan* **11**, 1104–1108.

Taylor, T. D. & Acrivos, A. 1964 On the deformation and drag of a falling viscous drop at low Reynolds number. *J. Fluid Mech.* **18**, 466–476.

Whitaker, S. 1972 Forced convection heat transfer correlations for flow in pipes, past flat plates, single cylinders, single spheres, and for flow in packed beds and tube bundles. *AIChE J.* **18**, 361–371.

White, B. R., Greeley, R., Iversen, J. D. & Pollack, J. B. 1976 Estimated grain saltation in a Martian atmosphere. *J. Geophys. Res.* **81**, 5643–5650.

Williams, J. C. 1977 Incompressible boundary-layer separation. *Ann. Rev. Fluid Mech.* **9**, 113–144.

Woo, S.-W. 1971 Simultaneous free and forced convection around submerged cylinders and spheres. Ph.D. thesis, McMaster University, Hamilton, Ontario.

Woo, S. E. & Hamielec, A. E. 1971 A numerical method of determining the rate of evaporation of small water drops falling at terminal velocity in air. *J. Atmos. Sci.* **28**, 1448–1454.